AIAA JOURNAL
Vol. 37, No. 12, December 1999

# Dispersion of Evaporating Droplets in a Swirling Axisymmetric Jet

S. K. Aggarwal* and T. W. Park†
*University of Illinois at Chicago, Chicago, Illinois 60607-7022*

**The effects of swirl and vaporization on droplet dispersion are investigated in the near region of a two-phase, swirling, heated jet. Simulations are based on the numerical solution of time-dependent, axisymmetric gas-phase equations. Droplets' trajectories are tracked by using a Lagrangian approach. For all of the swirl cases investigated, the droplet dispersion exhibits a nonmonotonic behavior, with the maximum dispersion occurring near Stokes number (St) unity. As the swirl intensity is increased, the radial dispersion of both nonevaporating and evaporating droplets is significantly enhanced. We attribute this dispersion enhancement to two factors: 1) increased vortex pairing interactions caused by swirl and 2) transfer of gas-phase swirl momentum to droplets. The effect of vaporization on dispersion is characterized in terms of droplet lifetime compared to its response time and the characteristic flow time. For the investigated conditions, the dispersion of evaporating droplets is noticeably reduced compared to that in the nonevaporating case. The dispersion function vs St behavior is also modified due to vaporization. Droplets with diameters smaller than the optimum value are sufficiently vaporized during their interaction with the vortex rings, and their dispersion approaches the low-St limit. On the other hand, droplets with diameters larger than the optimum are not vaporized significantly. Consequently, their dispersion follows the large-St behavior.**

## Nomenclature

| | |
|---|---|
| $C_D$ | = droplet drag coefficient |
| $D$ | = binary diffusion coefficient |
| $g$ | = gravitational acceleration |
| $H$ | = enthalpy |
| $h$ | = heat transfer coefficient, J/(m$^2$ · s$^{-1}$) |
| $\dot{m}_k$ | = droplet vaporization rate, $\pi d_k^2 \dot{m}_k''$ [Eq. (8)], kg/s |
| $p$ | = pressure |
| $Re_k$ | = droplet Reynolds number |
| $r$ | = radial distance |
| $S$ | = swirl number |
| $S_g^\Phi$ | = gas-phase source term for dependent variable $\Phi$ |
| $T$ | = temperature |
| $t$ | = time |
| $t_k$ | = droplet response time |
| $t_v$ | = droplet vaporization or lifetime |
| $u$, $v$, $w$ | = axial, radial, and swirl velocity components |
| $Y$ | = mass fraction |
| $z$ | = axial distance |
| $\Gamma^\Phi$ | = transport coefficient in Eq. (1) |
| $\rho$ | = density |
| $\Phi$ | = dependent variable in Eq. (1) |

*Subscripts*

| | |
|---|---|
| $f$ | = fuel vapor |
| $g$ | = gas phase |
| $k$ | = droplet |
| $s$ | = droplet surface |

## Introduction

IN recent years, numerous studies[1–6] have examined the effects of large-scale vortical structures on the dispersion of particles or droplets in shear flows. According to these studies, a key parameter characterizing droplet dispersion in shear flows is the Stokes number, defined as the ratio of a droplet response time to a characteristic flow time. The droplet response time $t_k$ is based on the Stokes drag law,[5] yielding $t_k = \rho_k d_k^2/18\mu$. The characteristic flow time $t_f$ is generally based on a timescale associated with the vortical structures; for example, it may be taken as the inverse of the fundamental (rollup) frequency or its subharmonic.[5] Both experimental and numerical investigations have shown that the presence of large vortex structures and their pairing interactions lead to a size-selective dispersion behavior such that the droplets with Stokes number near unity (St ~ 1.0) exhibit the maximum dispersion. Some recent studies[7–10] have also investigated the effects of acoustic forcing on droplet dispersion. These studies find that both the droplet dispersion and its concentration field can be modified significantly through an acoustic forcing of the shear layer. In general, periodic forcing at a subharmonic frequency can organize the spatio–temporal characteristics of large-scale structures in such a way that it leads to significantly higher droplet dispersion when compared to the unforced case. In addition, the dispersion gain is observed to have a size-selective behavior, with the maximum gain occurring near Stokes number of unity.

Previous studies dealing with droplet–vortex interactions have mostly focused on the dispersion of solid particles or nonevaporating droplets in shear flows.[1–10] Many practical spray systems, however, involve evaporating droplets, where the droplet diameter $d_k$ may decrease significantly during its interaction with a vortex. Consequently, the response time $t_k$ of an evaporating droplet may change significantly during its interaction with the vortex, because $t_k \sim d_k^2$, and modify its dispersion behavior. Then, in addition to the droplet response time and the vortex time (or eddy turnover time), the droplet lifetime becomes another relevant timescale for characterizing its dispersion behavior. For example, if the lifetime of a droplet in an evaporating spray is small compared to its response time, its dispersion behavior will be altered dramatically. This aspect has not been considered in previous studies, especially in the context of droplets interacting with large-scale structures.

Another aspect of droplet dynamics in shear flows deals with the effect of swirl on droplet dispersion. Swirling two-phase flows occur in numerous applications including spray combustion, where a swirl velocity component is imparted to either the carrier fluid, to the dispersed phase, or to both, primarily to enhance mixing and flame stability. Because droplet transport in these flows is strongly influenced by large-scale motions, it is clearly of interest to examine the effects of swirl on vortex ring dynamics and droplet transport. The

Received 22 June 1998; revision received 13 January 1999; accepted for publication 20 April 1999. Copyright © 1999 by S. K. Aggarwal and T. W. Park. Published by the American Institute of Aeronautics and Astronautics, Inc., with permission.

*Professor, Department of Mechanical Engineering (M/C 251), 842 W. Taylor Street; ska@uic.edu. Associate Fellow AIAA.

†Research Assistant, Department of Mechanical Engineering (M/C 251), 842 W. Taylor Street; currently Research Engineer, AYT Corporation, NASA John H. Glenn Research Center at Lewis Field, Brook Park, OH 44142. Member AIAA.

presence of swirl in a two-phase jet can affect droplet dynamics in two ways. First, it modifies the spatial and temporal characteristics of large-scale structures because a swirling jet is subjected to both shear and centrifugal instabilities. Any modifications in the dynamics of large-scale structures, such as their rollup location, frequency, and pairing interactions, will have a noticeable effect on the droplet dynamics and vaporization. Second, the presence of swirl imparts radial acceleration to droplets, modifying their motion and dispersion behavior. To the best of our knowledge, these effects have not been addressed in previous investigations, which have focused on the time-averaged behavior of single-phase[11–13] and two-phase[14–16] swirling jets. In particular, the dynamics of vortex rings and its influence on droplet dispersion in the near region of a swirling jet have not been investigated in previous studies.

The present numerical study is motivated by the preceding considerations. A time-dependent, axisymmetric, two-phase algorithm is employed to examine the dispersion of nonevaporating and evaporating droplets in a swirling heated jet. Using detailed flow visualizations and quantitative results, the effects of swirl and vaporization on droplet dispersion are characterized. Note that in a previous study,[17] we simulated the dynamics of large-scale vortex structures in a swirling jet and examined the momentum coupling effects of the dispersed phase (nonevaporating droplets) on the jet spatio–temporal characteristics. The present study, on the other hand, examines the effects of large-scale structures on the dynamics and dispersion of evaporating droplets in a swirling jet.

## Physical–Numerical Model

The physical model considers a droplet-laden swirling jet in an annular airflow. The jet diameter is 25.0 mm, axial velocity is 5.0 m/s, and temperature is 1200 K, whereas the coflow is at a velocity of 0.2 m/s and a temperature of 294 K. The use of high jet temperature stems from the consideration that the dispersion of both nonevaporating and evaporating droplets is studied. The choice of 1200 K as the jet temperature yields a droplet lifetime (based on a droplet diameter of 100 $\mu$m) comparable to the flow and droplet timescales; see Table 1. Compared to this case, two other cases, for which the droplet lifetime is either much smaller or much larger than the flow and droplet timescales, are not as interesting. In the former, the evaporating droplets would behave like gas particles, whereas in the latter, they would behave like nonevaporating droplets. The jet Reynolds number, based on air properties at a temperature of 1200 K, is 800.

The swirl is imparted to the central jet by specifying a linear swirl velocity profile at the inflow boundary, that is, by considering swirl velocity as a linear function of radial location. The swirl intensity is characterized in terms of a nondimensional swirl number, which represents the ratio of swirl momentum flux to axial momentum flux in the jet and is given by

$$S = \frac{1}{r_0}\left( \int_0^{r_0} uwr^2 \, \mathrm{d}r \Big/ \int_0^{r_0} u^2 r \, \mathrm{d}r \right) \tag{1}$$

where $r_0$ is the radial extent of the computational domain. This definition treats $S$ as a function of axial distance. Thus, at the inflow boundary $r_0$ becomes equal to the jet radius.

The shear-layer dynamics in the near region of a swirling jet is dominated by the Kelvin–Helmholtz vortex rings and is simulated by solving the time-dependent, gas-phase equations in an axisymmetric geometry without any turbulence or subgrid model. These equations in cylindrical $(z, r)$ coordinates can be written as

$$\frac{\partial(\rho\Phi)}{\partial t} + \frac{\partial(\rho u\Phi)}{\partial z} + \frac{\partial(\rho v\Phi)}{\partial r} = \frac{\partial}{\partial z}\left(\Gamma^{\Phi}\frac{\partial\Phi}{\partial r}\right) + \frac{\partial}{\partial r}\left(\Gamma^{\Phi}\frac{\partial\Phi}{\partial z}\right) - \frac{\rho v\Phi}{r} + \frac{\Gamma^{\Phi}}{r}\frac{\partial\Phi}{\partial r} + S_g^{\Phi} \tag{2}$$

The general form of Eq. (2) represents the continuity, the three momentum, and the energy conservation equations, depending on the variable used for $\Phi$. The transport coefficients $\Gamma^{\Phi}$ and the source term $S_g^{\Phi}$ that appear in the governing equations are listed in Table 2. Note that there is an extensive body of research, both experimental[11,12] and computational,[13,14] to justify the axisymmetric flow assumption for a swirling jet. The transport coefficients $\Gamma^{\Phi}$ and source terms contain the fluid properties such as viscosity, thermal conductivity, and specific heat. They are considered functions of temperature and species concentration. Note that a one-way coupled system is considered. Consequently, the dispersed-phase source terms in the gas-phase equations that represent the effect of dispersed phase on the gas flow are not included in Table 2. This is justified because the mass loading, defined as the ratio of liquid mass flow rate to gas mass flow rate, is less than 0.001.

The numerical solution of the preceding equations is based on the methodology developed by Katta et al.[18] for solving the variable-density flow equations. The finite difference forms of the momentum equations are obtained using an implicit QUICKEST scheme,[19] whereas those of energy equations are obtained using a hybrid scheme of upwind and central differencing.[20] A finite control volume approach with a nonuniform staggered-grid system is utilized. An orthogonal grid having expanding cell sizes in both the axial and the radial direction is employed. An iterative alternating direction implicit technique is used for solving the resulting sets of algebraic equations. At every time step, the pressure field is calculated by solving all of the pressure Poisson equations simultaneously and utilizing the lower and upper diagonal matrix decomposition technique.

Axisymmetric calculations are made on a physical domain of $400 \times 150$ mm utilizing a $151 \times 61$ nonuniform grid system. The computational domain is bounded by the axis of symmetry (left boundary) and an outflow (right) boundary in the radial direction and by the inflow (bottom) and another outflow (top) boundary in the axial direction. The outer boundaries in the $z$ and $r$ directions are located sufficiently far from the nozzle exit (16 nozzle diameters) and the axis of symmetry (6 nozzle diameters), respectively, to minimize the propagation of boundary-induced disturbances into the region of interest (7 and 2 nozzle diameters in the axial and radial directions, respectively). A flat profile for axial velocity and a linear profile for swirl velocity are used at the inflow boundary. A zero-gradient boundary condition with an extrapolation procedure with weighted zero- and first-order terms is used to estimate the flow variables at the outflow boundary.[18] The weighting functions are selected using the trial-and-error approach, and the main criterion used is that the vortices crossing the outflow boundary leave smoothly without being distorted. The flow entrainment from the right boundary into the computational region is also properly accounted for in the boundary condition. For the given flow conditions, a steady-state solution was first obtained by neglecting the unsteady terms in the

**Table 1 Response time $t_k$, vaporization time $t_v$, and Stokes numbers for various droplet diameters for both nonswirling and swirling jets**

| $d_k$, $\mu$m | $t_k$, ms | $t_v$, ms (%) | St ($S = 0.0$), $t_f = 15.6$ ms | St ($S = 0.375$), $t_f = 13.9$ ms | St ($S = 0.5$), $t_f = 12.5$ ms |
|---|---|---|---|---|---|
| 25 | 0.67 | 1.45 (90) | 0.043 | 0.048 | 0.053 |
| 50 | 2.67 | 5.72 (90) | 0.17 | 0.19 | 0.21 |
| 100 | 10.67 | 25.72 (70) | 0.68 | 0.77 | 0.85 |
| 125 | 16.68 | 36.50 (55) | 1.07 | 1.20 | 1.33 |
| 150 | 24.02 | 41.20 (30) | 1.54 | 1.73 | 1.92 |
| 175 | 32.69 | 47.20 (25) | 2.09 | 2.35 | 2.62 |
| 200 | 42.69 | 53.34 (20) | 2.73 | 3.07 | 3.42 |

**Table 2 Transport coefficients and source terms appearing in gas-phase governing equations**

| Equations | $\Phi$ | $\Gamma^{\Phi}$ | $S_g^{\Phi}$ |
|---|---|---|---|
| Continuity | 1 | 0 | 0 |
| Axial momentum | $u$ | $\mu$ | $-\frac{\partial p}{\partial z}+(\rho_0-\rho)g+\frac{\partial}{\partial z}\left(\mu\frac{\partial u}{\partial z}\right)+\frac{\partial}{\partial r}\left(\mu\frac{\partial v}{\partial z}\right)+\frac{\mu}{r}\frac{\partial v}{\partial z}$ $-\frac{2}{3}\left[\frac{\partial}{\partial z}\left(\mu\frac{\partial u}{\partial z}\right)+\frac{\partial}{\partial z}\left(\mu\frac{\partial v}{\partial r}\right)+\frac{\partial}{\partial z}\left(\mu\frac{v}{r}\right)\right]$ |
| Radial momentum | $v$ | $\mu$ | $-\frac{\partial p}{\partial r}+\frac{\partial}{\partial z}\left(\mu\frac{\partial u}{\partial r}\right)+\frac{\partial}{\partial r}\left(\mu\frac{\partial v}{\partial r}\right)+\frac{\mu}{r}\frac{\partial v}{\partial r}-2\mu\frac{v}{r^2}$ $+\rho\frac{w^2}{r}-\frac{2}{3}\left[\frac{\partial}{\partial r}\left(\mu\frac{\partial u}{\partial z}\right)+\frac{\partial}{\partial r}\left(\mu\frac{\partial v}{\partial r}\right)+\frac{\partial}{\partial r}\left(\mu\frac{v}{r}\right)\right]$ |
| Swirl momentum | $w$ | $\mu$ | $-\left(\frac{\mu}{r^2}+\rho\frac{v}{r}+\frac{1}{r}\frac{\partial\mu}{\partial r}\right)w$ |
| Mass fraction of fuel | $Y_f$ | $\rho D_{f-N_2}$ | 0 |
| Mass fraction of other species | $Y_i$ $(i=1\sim N_s, i\neq f)$ | $\rho D_{i-N_2}$ | 0 |
| Energy | $H$ | $\lambda/C_p$ | 0 |

governing equations. Then, the unsteady swirling jet simulations were performed using the previously obtained steady-state solution as the initial flow condition.

To examine the effects of swirl and vaporization on droplet dispersion, n-heptane fuel droplets of specified diameter and velocity are injected into the swirling jet shear layer, and their trajectories are tracked by following a Lagrangian approach. The equations governing the variation of position and velocity of each droplet in a swirling flow are as follows:

$$\frac{\mathrm{d}x_k}{\mathrm{d}t}=u_k \tag{3}$$

$$\frac{\mathrm{d}y_k}{\mathrm{d}t}=v_k$$

$$\frac{\mathrm{d}u_k}{\mathrm{d}t}=\frac{3C_D\rho_g}{4d_k\rho_k}|u_g-u_k|(u_g-u_k)+\left(\frac{\rho_g}{\rho_k}-1\right)g \tag{4}$$

$$\frac{\mathrm{d}v_k}{\mathrm{d}t}=\frac{3C_D\rho_g}{4d_k\rho_k}|v_g-v_k|(v_g-v_k)+\frac{w_k^2}{y_k}$$

$$\frac{\mathrm{d}w_k}{\mathrm{d}t}=\frac{3C_D\rho_g}{4d_k\rho_k}|w_g-w_k|(w_g-w_k)-\frac{v_kw_k}{y_k}$$

where

$$C_D=\frac{24}{Re_k}\left(1+\frac{Re_k^{\frac{2}{3}}}{6}\right)(1+B)^{-0.2} \tag{5}$$

$$Re_k=\frac{\rho_g\left\{(u_g-u_k)^2+(v_g-v_k)^2+(w_g-w_k)^2\right\}^{\frac{1}{2}}d_k}{\mu_g} \tag{6}$$

Note that at a pressure equal to 1 atm, the ratio of liquid to air density is about 580. This sufficiently large density ratio allows us to neglect the Basset force, pressure gradients, and other contributions from flow nonuniformities and to consider only the drag force in Eq. (4). Moreover, using a scale analysis, Lazaro and Lasheras[21] have identified the conditions when these additional forces can be neglected. These conditions are also applicable to our study. The droplet–droplet interaction is also neglected in this analysis because an ultradilute two-phase flow is being simulated. For all of the cases simulated, the droplet mass loading ratio is less than 0.001, which yields a void fraction of about $10^{-6}$. However, the effect of Stefan flow (blowing) on the droplet drag is included [see Eq. (5)] following recommendations of Renksizbulut and Yuen[22] and Sirignano.[23] The following expressions[23] are used for heat and mass transfer rates to the droplet:

$$\frac{hd_k}{\lambda}=\frac{2(N_p/Le)\ln(1+B)}{(1+B)^{1/Le}-1} \tag{7}$$

$$\frac{\dot{m}_k''d_k}{\rho D}=2N_s\ln(1+B) \tag{8}$$

where $B$ is the Spalding transfer number given by

$$B=\frac{Y_{Fs}-Y_{F\infty}}{1-Y_{Fs}} \tag{9}$$

and $N_p$ and $N_s$, corrective factors accounting for the convective effect on heat and mass transfer, are calculated using semi-empirical relations[24]:

$$N_P \text{ or } N_S=1+\frac{0.278Re_k^{\frac{1}{2}}(Pr \text{ or } Sc)^{\frac{1}{3}}}{\left[1+1.232/(Re_k(Pr \text{ or } Sc)^{\frac{4}{3}}\right]^{\frac{1}{2}}} \tag{10}$$

To complete the solution, the temperature and fuel mass fraction at the droplet surface must be known. The two equations used to solve for these quantities are provided by the fuel vapor pressure relationship and the liquid-phase energy equation in the droplet interior. The vapor pressure relationship has the form

$$Y_{Fs}=f(T_s, P, Y_{is}) \tag{11}$$

In the droplet vaporization model used here, the effect of transient heating is incorporated through the conduction-limit model, such that the transient heat transport within the droplet is represented by the unsteady heat diffusion equation in a spherically symmetric geometry. The details of this equation are provided in an earlier study.[25] The vapor pressure relationship and other properties used for the liquid and gas phases are also provided in Ref. 25. The droplet model includes the effects of variable thermophysical properties and nonunity Lewis number in the gas film outside the droplet. The thermophysical properties are calculated at an average reference state defined as

$$\Phi_{\mathrm{av}}=\alpha\Phi_{gs}+(1-\alpha)\Phi_g \tag{12}$$

where $\Phi$ represents either mass fraction or temperature and $\alpha$ is selected to be 0.7. The subscripts $gs$ and $g$ represent the gas-phase property at the droplet surface and outside the gas film, respectively.

The preceding equations governing the position and velocity of each droplet are advanced in time by an explicit second-order Runge–Kutta method. Because the gas-phase solution employs an implicit procedure, the temporal step size used for integrating the droplet equations is usually smaller than that for gas-phase equations. An automatic procedure is implemented to select an optimum time step for the droplet equations.

Numerical validation studies for nonswirling jets employing different grids and temporal step sizes have been reported previously.[25] These studies also established that the numerical model reproduces the spatio–temporal characteristics of large-scale structures in nonswirling jets. For swirling jets, additional results[17] showing grid

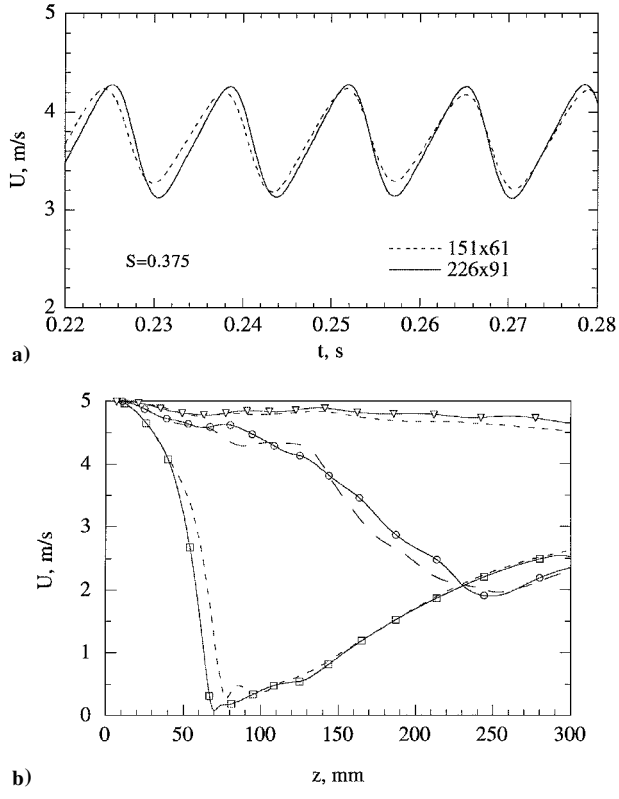


**Fig. 1 Nonswirling and swirling jets ($S = 0.375$ and 0.5) results obtained using two different grids: a) time history of axial gas velocity at a location $z = 2.0$ cm, $r = 1.27$ cm in a swirling jet and b) variation of time-averaged axial gas velocity along the jet centerline: – – –, 151 × 61 ($S = 0$); ▽, 226 × 91 ($S = 0$); — —, 151 × 61 ($S = 0.375$); ○, 226 × 91 ($S = 0.375$); · · · · · ·, 151 × 61 ($S = 0.5$); and □, 226 × 91 ($S = 0.5$).**

independence are shown in Fig. 1. The time history of axial gas velocity for two different grids, $151 \times 61$ and $226 \times 91$, is shown in Fig. 1a, whereas the time-averaged axial velocity along the jet axis for different swirl numbers is plotted in Fig. 1b. Because a nonuniform grid is employed with grid lines clustered near the shear layer to resolve the steep gradients of the dependent variables, additional grid points in the $226 \times 91$ grid are placed near the shear layer, thus effectively reducing the grid density for this grid by about 100% compared to the $151 \times 61$ grid. The time-history plots of gas velocity clearly show the highly periodic nature of jet vortex rings associated with the Kelvin–Helmholtz instability. For the nonswirling jet, the computed Strouhal number associated with this instability obtained from the fast Fourier transform of the axial velocity was 0.32, which agreed with the reported experimental range of 0.25–0.5. The computed Strouhal number for the swirling jets was observed to be higher, increasing to 0.36 for $S = 0.375$ and to 0.4 for $S = 0.5$. An important observation regarding the grid independence is that the $151 \times 61$ grid is able to capture the periodic behavior, including frequency and phase of the vortex structures, as well as the time-averaged structure of both nonswirling and swirling jets.

## Results

Results focus on the effects of swirl and vaporization on the dynamics of droplets as they interact with large vortex rings in a swirling jet. As discussed earlier, a swirling jet is subjected to both shear and centrifugal instabilities. Consequently, the spatio–temporal characteristics of large-scale structures may be modified significantly, which can alter the droplet dispersion and distribution behavior. The presence of swirl also imparts an azimuthal velocity to droplets, due to the swirl momentum transfer from the gas phase. This in turn provides radial acceleration [see Eq. (4)] to their motion, causing them to disperse radially. In addition, the dispersion behavior of evaporating droplets is modified due to a reduction in their size. To examine these effects qualitatively, we inject different-sized droplets into the jet shear layer and follow their trajectories and distribution by using flow visualization based on snapshots (instantaneous images) of the two-phase flow. Figure 2 shows several such snapshots for different droplet sizes and swirl numbers. In each snapshot, the instantaneous isotemperature contours and droplet locations are plotted for both nonevaporating and evaporating droplets for three different droplet sizes. To examine the effect of vaporization on droplet dispersion, instantaneous locations of evaporating and nonevaporating droplets are plotted on the left-hand and right-hand sides of the symmetric jet, respectively. Color representing the size of the droplet changes from red to blue as it evaporates from the initial size (at the instant of injection) to the size of a gas (tracer) particle, which is taken as 10 $\mu$m or $\frac{1}{10}$th of the initial size, whichever is smaller. Because the droplets on the left-hand side of the jet represent nonevaporating ones, the color of the droplets remains red.

Snapshots for the nonswirling case (Fig. 2a) indicate a nonmonotonic dispersion behavior for both nonevaporating and evaporating droplets, though it is more easily discernible for the former. As discussed in previous experimental[1,2] and numerical studies,[3,4] the nonmonotonic behavior, whereby the intermediate size nonevaporating droplets (Stokes number near unity) are dispersed the most, is a result of the interaction of droplets with vortex rings and is characterized by a Stokes number. Whereas small droplets (small Stokes number) are caught in the vortex rings and large droplets (large Stokes number) pass through them, the intermediate size droplets (Stokes number near unity) are trapped into and then flung out of them. From snapshots in Fig. 2a, one infers that 50- and 100-$\mu$m nonevaporating droplets exhibit intermediate Stokes number behavior as they are distributed around the vortex rings and in the braid region between them, whereas 150-$\mu$m nonevaporating droplets exhibit large Stokes number behavior. In contrast, 50-, 100-, and 125-$\mu$m (not shown) evaporating droplets are mostly distributed inside the vortex rings, implying small Stokes number behavior, because they vaporize significantly during their interaction with the first three vortex rings. Some representative values of the droplet response time and vaporization time as well as of Stokes numbers are provided in Table 1. For the droplet response time ($t_k = \rho_k d_k^2/18\mu_g$) (Table 1), the droplet density $\rho_k = 649.38$ kg/m$^3$, and the gas viscosity $\mu_g = 3.38 \times 10^{-5}$ kg/m calculated at a mean gas temperature of 747 K. For evaporating droplets, the droplet response time is based on the initial diameter. The characteristic flow time or the vortex time $t_f$ is based on the fundamental frequency for each case, obtained from the fast Fourier transform of the gas-phase axial velocity history. These frequencies are 64, 72, and 80 Hz for $S = 0$, 0.375, and 0.5, respectively. The vaporization times $t_v$ (Table 1) correspond to at least a 50% reduction in droplet diameter for 25-, 50-, 100-, and 125-$\mu$m droplets. However, the reduction is only 30, 25, and 20%, respectively, for 150-, 175-, and 150-$\mu$m droplets. The inference is that, for the conditions considered, droplets with initial diameter smaller than 125 $\mu$m vaporize significantly, whereas droplets with initial diameter larger than 150 $\mu$m do not vaporize appreciably during their interaction with the vortex rings. As indicated in Table 1, the vaporization times for 50-, 100-, and 125-$\mu$m droplets are of the order of the vortex time. Consequently, their dispersion is modified significantly by vaporization and becomes similar to that of gas particle, that is, it follows small Stokes number behavior. The snapshots for 150- and 200-$\mu$m (latter not shown) evaporating droplets indicate a large Stokes number behavior, which is not significantly affected by vaporization.

The described dispersion behavior becomes more perceptible in Fig. 3a, where we present quantified results, corresponding to the snapshots of Fig. 2a, by plotting dispersion function as a function of time for nonevaporating and evaporating droplets. The dispersion function that measures the average radial displacement of droplets is defined[1–4] as

$$D(t, N) = \left\{ \sum_{i=1}^{N} [r_i(t) - r_{i0}]^2 / N \right\}^{\frac{1}{2}} \tag{13}$$

where $N$ is the total number of droplets in the flowfield at time $t$, $r_i$ the radial location of droplet $i$ at time $t$, and $r_{i0}$ the radial injection location of the same droplet at injection location.

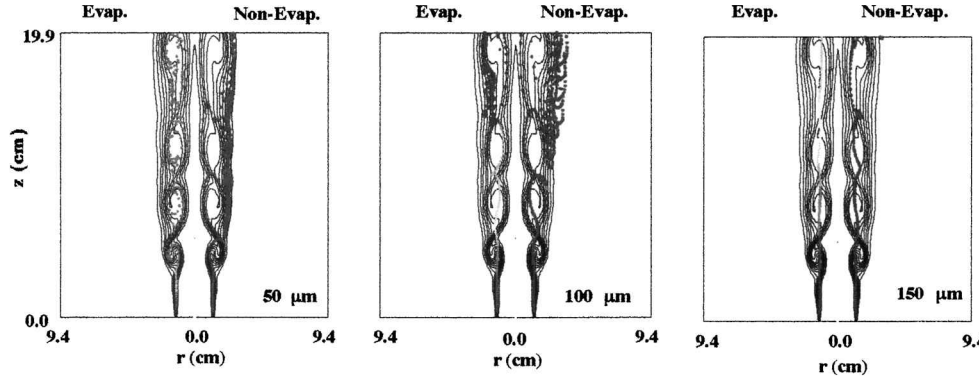


a) Nonswirling case

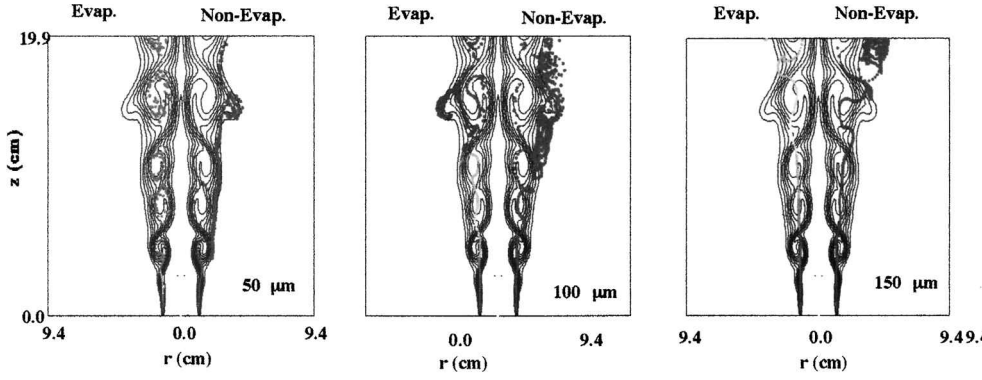


b) Swirl number 0.25

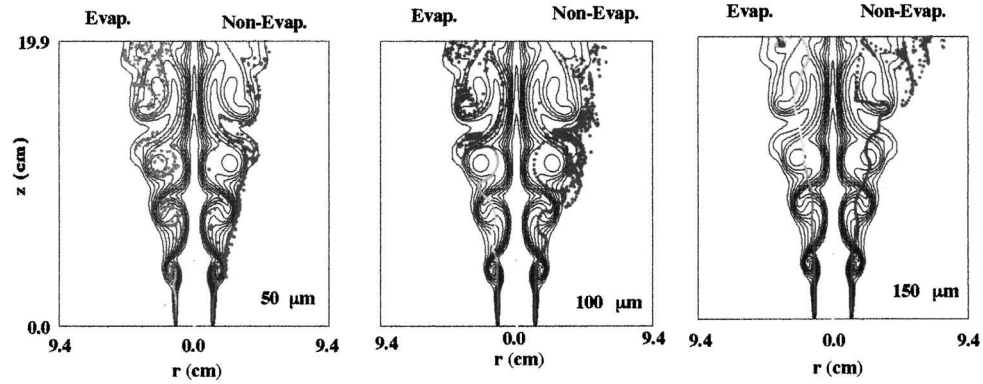


c) Swirl number 0.375

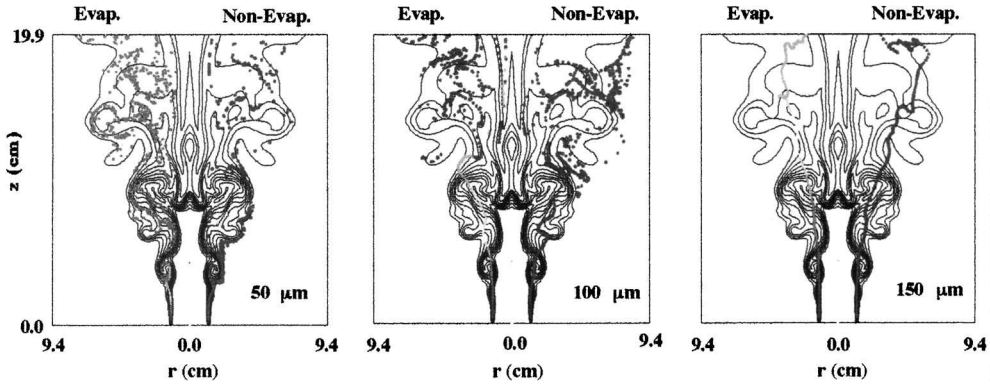


d) Swirl number 0.5

**Fig. 2 Snapshots (computed images) of the two-phase flowfield in terms of the instantaneous isotemperature contours and droplet locations of both nonevaporating and evaporating droplets.**

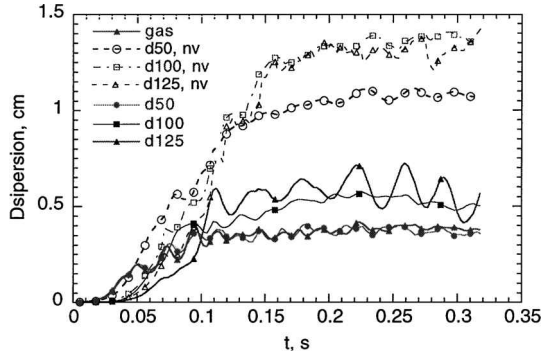


a) $S = 0$

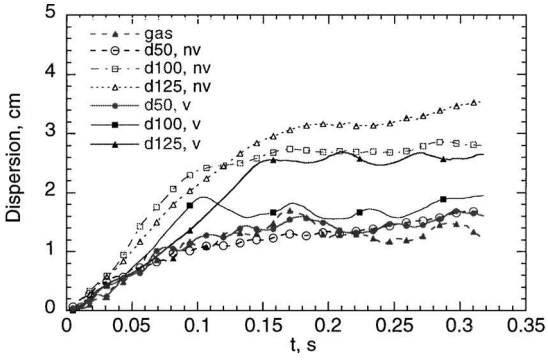


b) $S = 0.375$

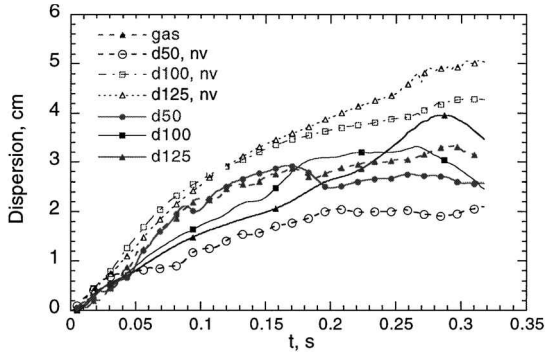


c) $S = 0.5$

**Fig. 3 Temporal variation of dispersion function for nonevaporating (nv) and evaporating (v) droplets of different initial droplet diameters.**

The dispersion function plots in Fig. 3a essentially confirm the qualitative results presented in Fig. 2a. The dispersion function for nonevaporating droplets indicates a typical nonmonotonic behavior such that the intermediate-size droplets (50, 100, and 125 $\mu$m) are dispersed more than the gas particles. This behavior is, however, modified significantly for evaporating droplets. As discussed earlier, the 50-, 100-, and 125-$\mu$m droplets undergo significant vaporization during their interaction with the vortex rings because their vaporization time is on the order of the vortex time. Consequently, as shown in Fig. 3a, their dispersion follows gas dispersion or small Stokes number behavior. The larger droplets on the other hand are not sufficiently vaporized and, thus, exhibit large Stokes number behavior. Note that the vaporization time of larger droplets increases due to two effects: 1) It varies as square of the droplet diameter. 2) These droplets are transported into the colder region (see Fig. 2a) as the gas temperature decreases in the axial direction.

**Effect of Swirl on Dispersion**

The qualitative effects of swirl on droplet dispersion are shown in Figs. 2b–2d. These snapshots provide clear evidence that swirl has a strong effect on the dynamics of two-phase flow. Not only does it modify the dynamics of vortex rings and jet mixing behavior, it also alters the dispersion of nonevaporating and evaporating droplets. As the swirl intensity is increased, it enhances the radial dispersion

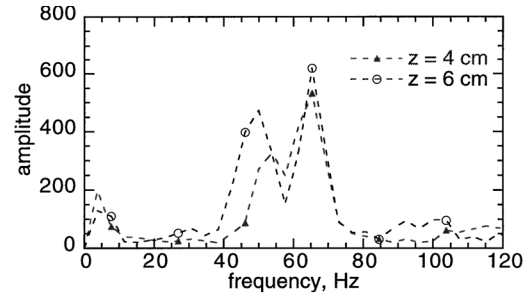


$S = 0$

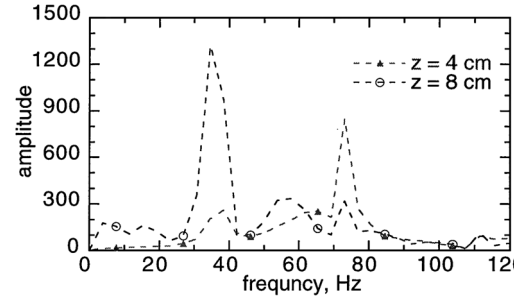


$S = 0.375$

**Fig. 4 Fourier spectra of axial gas-phase velocity for nonswirling ($S = 0$) and swirling ($S = 0.375$) jets.**

of droplets over the entire droplet diameter range. More detailed flow visualization, including an animation of the two-phase flow, indicated that, with increasing swirl, the vortex rings grow radially in size, their rollup frequency increases, and they undergo stronger pairing interactions. The increased vortex size and stronger pairing interactions are easily discernible in Figs. 2b and 2c. The effects of swirl on the vortex frequency and pairing interactions are shown in Fig. 4, where we plot the Fourier spectra of axial velocity history recorded at two axial locations for $S = 0$ and 0.375. As indicated, the rollup frequencies are 64 and 72 Hz for $S = 0$ and 0.375, respectively, and there is a strong vortex pairing with a frequency of 36 Hz for $S = 0.375$. The increased vortex size is probably attributable to the higher gas-phase radial velocity caused by swirl because the azimuthal (swirl) velocity appears as a source term in the gas-phase radial momentum equation (see Table 2). The strong pairing interactions on the other hand are caused by the adverse pressure gradient generated by the presence of swirl. The adverse pressure gradient reduces the axial gas-phase velocity in the downstream direction (see Fig. 1b). As a result, the leading vortex is slowed down, causing a well-organized pairing interaction to occur near $z = 7$ cm.

The quantitative results showing the effects of swirl on droplet dispersion are given in Figs. 3b and 3c. Important observations are as follows:

1) The comparison of dispersion plots for the swirling and nonswirling cases indicate that swirl significantly enhances droplet dispersion over the entire diameter range. Note the maximum dispersion increases from about 1.5 cm (for $S = 0$) to 3 cm for $S = 0.375$ and to 5 for $S = 0.5$. These results are in accord with snapshots given in Figs. 2a–2d.

2) For $S = 0.375$, the dispersion of 50-$\mu$m nonevaporating droplets is nearly the same as that of gas particles, whereas for $S = 0.5$, it is lower than that of gas particles. This is in contrast to the nonswirling case (Fig. 3a) for which the 50-$\mu$m droplets disperse more than the gas particles. This means an increasing swirl intensity causes relatively greater enhancement in gas particle dispersion compared to that of 50-$\mu$m droplets, implying that swirl significantly increases gas-phase mixing.

3) For all of the swirl cases investigated, the dispersion of 100- and 125-$\mu$m nonevaporating droplets exhibits intermediate Stokes number behavior, whereas that of larger droplets exhibits large Stokes number behavior.

4) In contrast to the nonevaporating case, the dispersion of 100- and 125-$\mu$m evaporating droplets is similar to that of gas particles, that is, it follows small Stokes number behavior for all of the swirl

cases investigated. As discussed earlier, this implies significant vaporization for these droplets during their interaction with vortex rings. Larger evaporating droplets ($d_k \geq 150\,\mu$m) on the other hand exhibit large Stokes number behavior.

Another way of elucidating the effects of swirl on droplet dispersion is to plot the temporal variation of dispersion function using $S$ as a parameter. Figure 5a shows this plot for the dispersion of gas particles. As $S$ is increased, the gas particle dispersion is significantly enhanced, providing further evidence of increased vortex size and stronger pairing interactions at higher swirl numbers. In addition, as noted earlier in Fig. 2d, there is a sharp increase in the jet spreading angle for $S = 0.5$, accompanied by a significantly higher rate of shear layer growth. Figure 5a provides further evidence of this, as there is a sharp increase in the gas particle dispersion function for $S = 0.5$. The enhanced gas dispersion in a swirling jet can be attributed to two effects. First, the swirl velocity appears as a source term in the gas-phase radial momentum equation (Table 2) and contributes directly to higher radial dispersion. Second, the swirl induces an adverse pressure gradient in the axial direction, which leads to strong vortex mergings and higher gas dispersion.

Figures 5b–5d show the effect of swirl on the dispersion of 50-, 100-, and 200-$\mu$m droplets, respectively. The important observation is that the presence of swirl enhances the radial dispersion of both nonevaporating and evaporating droplets over the entire droplet size range. Note from Fig. 5b that swirl causes a relatively greater increase in the dispersion of 50-$\mu$m evaporating droplets compared to that of nonevaporating droplets. This is directly related to the observation made earlier that the dispersion of 50-$\mu$m evaporating droplets follows the gas particle behavior and that swirl enhances the dispersion of gas particles more than that of 50-$\mu$m nonevaporating droplets. A similar behavior is observed for 100-$\mu$m droplets, that is as $S$ is increased it increases the dispersion of evaporating droplets more than that of nonevaporating droplets. For larger droplets ($d_k \geq 150\,\mu$m), there is essentially no difference in regard to the relative effect of swirl on the dispersion of nonevaporating and evaporating droplets. This is again because these droplets follows the large Stokes number behavior, which is not much affected by vaporization, as their vaporization time is much greater than the vortex time.

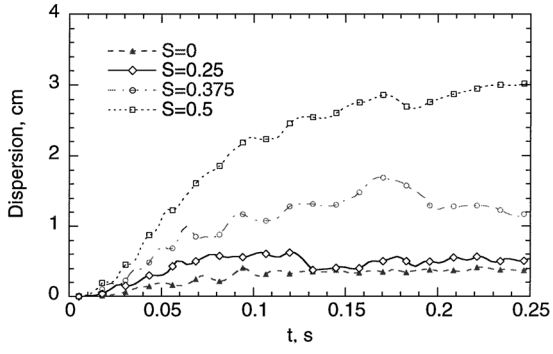


**a) Gas or tracer particles**

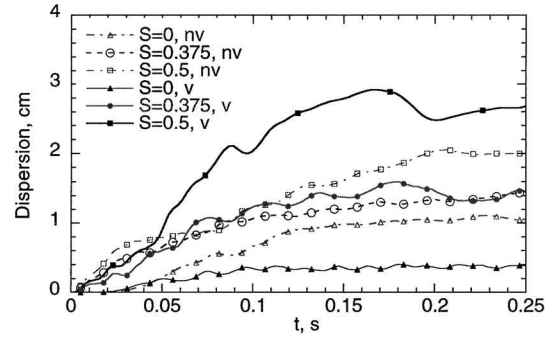


**b) Initial droplet diameter 50 $\mu$m**

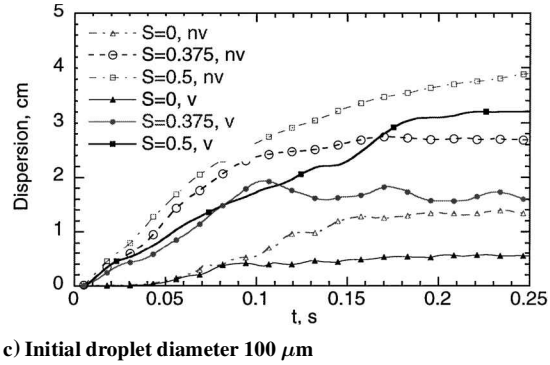


**c) Initial droplet diameter 100 $\mu$m**

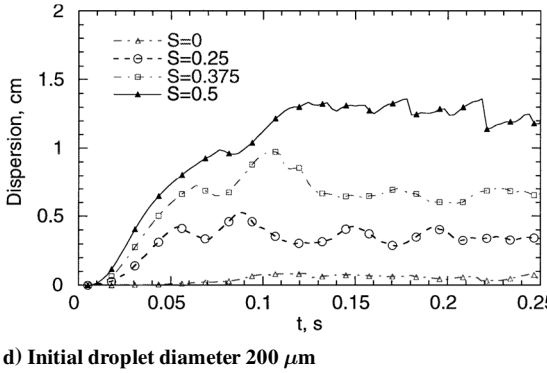


**d) Initial droplet diameter 200 $\mu$m**

**Fig. 5 Dispersion function vs time for nonevaporating (nv) and evaporating (v) droplets for different swirl numbers.**

**Dispersion Function vs Droplet Stokes Number**

The effects of droplet size on dispersion is often characterized by plotting the dispersion function as a function of droplet diameter or Stokes number. Figures 6 and 7 show such plots for both nonevaporating and evaporating cases at different swirl numbers. For these results, the simulations are performed over 20 vortex periods, and the dispersion function is averaged over the last vortex period, that

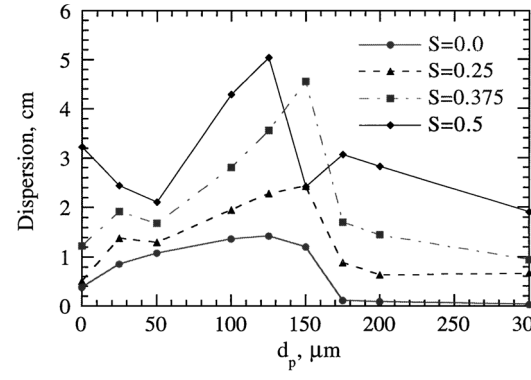


**Nonevaporating droplets**

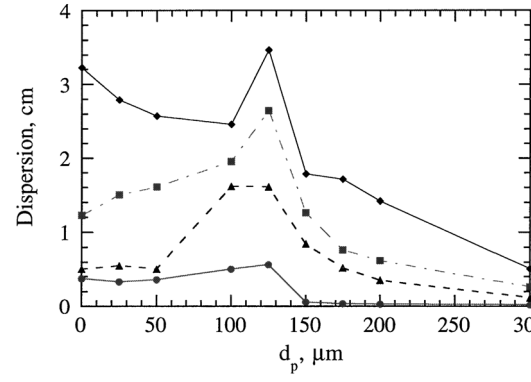


**Evaporating droplets**

**Fig. 6 Dispersion function vs initial droplet diameter for nonswirling and three swirling cases.**

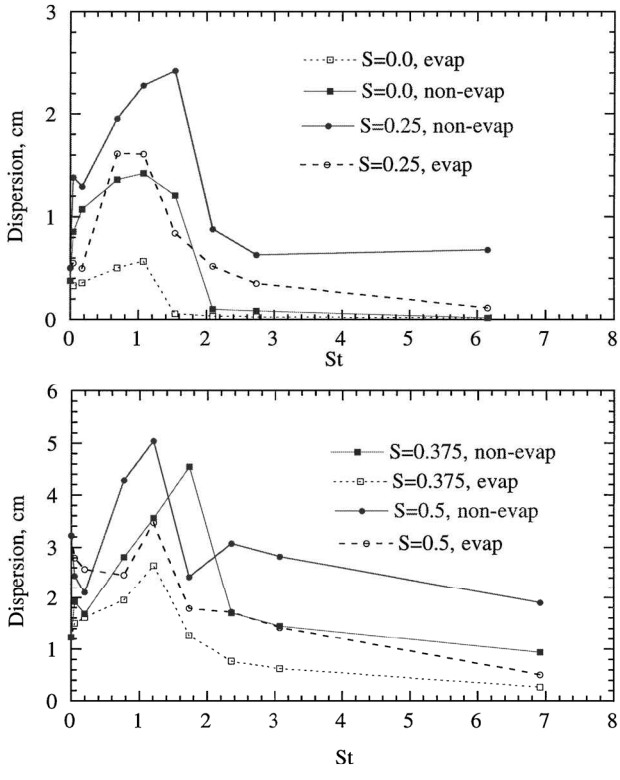


**Fig. 7 Dispersion function for nonevaporating and evaporating droplets plotted vs the Stokes number for nonswirling and three swirling cases.**

is, near the end of computations. At the end of computations, there are 2000 droplets for the calculation of the dispersion function. For sufficiently long computational time and number of droplets, the dispersion function results are shown to be independent of these parameters.[4,10] Important observations are as follows:

1) For all of the swirl cases investigated, the dispersion function exhibits a nonmonotonic behavior, with a maximum value occurring near droplet diameter 125–150 $\mu$m (Fig. 6), corresponding to a Stokes number near unity (see Fig. 7). Thus, the droplet size corresponding to the maximum dispersion is nearly independent of the swirl number. Also, it is not affected much by vaporization.

2) As the swirl number is increased, the dispersion of both nonevaporating and evaporating droplets increases over the entire Stokes number (droplet size) range. As discussed earlier, the enhancement is caused by two effects: stronger vortex pairings (and enhanced shear-layer growth rate) at higher swirl number and transfer of the gas-phase swirl momentum to the dispersed phase.

3) The dispersion of evaporating droplets is significantly reduced compared to that of nonevaporating droplets. This is shown more clearly in Fig. 7, which shows the dispersion function of nonevaporating and evaporating droplets vs the Stokes number for different swirl numbers. Note that the Stokes number for evaporating droplets is based on their initial diameter. As discussed earlier, the droplets with diameter less than the optimum value (corresponding to the maximum dispersion) are sufficiently vaporized so that their dispersion behavior approaches the small Stokes number limit. On the other hand, the droplets with diameter higher than the optimum value are not vaporized significantly. Consequently, the dispersion of large nonevaporating and evaporating droplets follows the large Stokes number behavior, though their relative dispersion is reduced for the latter case. As indicated in Fig. 7, this behavior is observed for all of the swirl cases investigated.

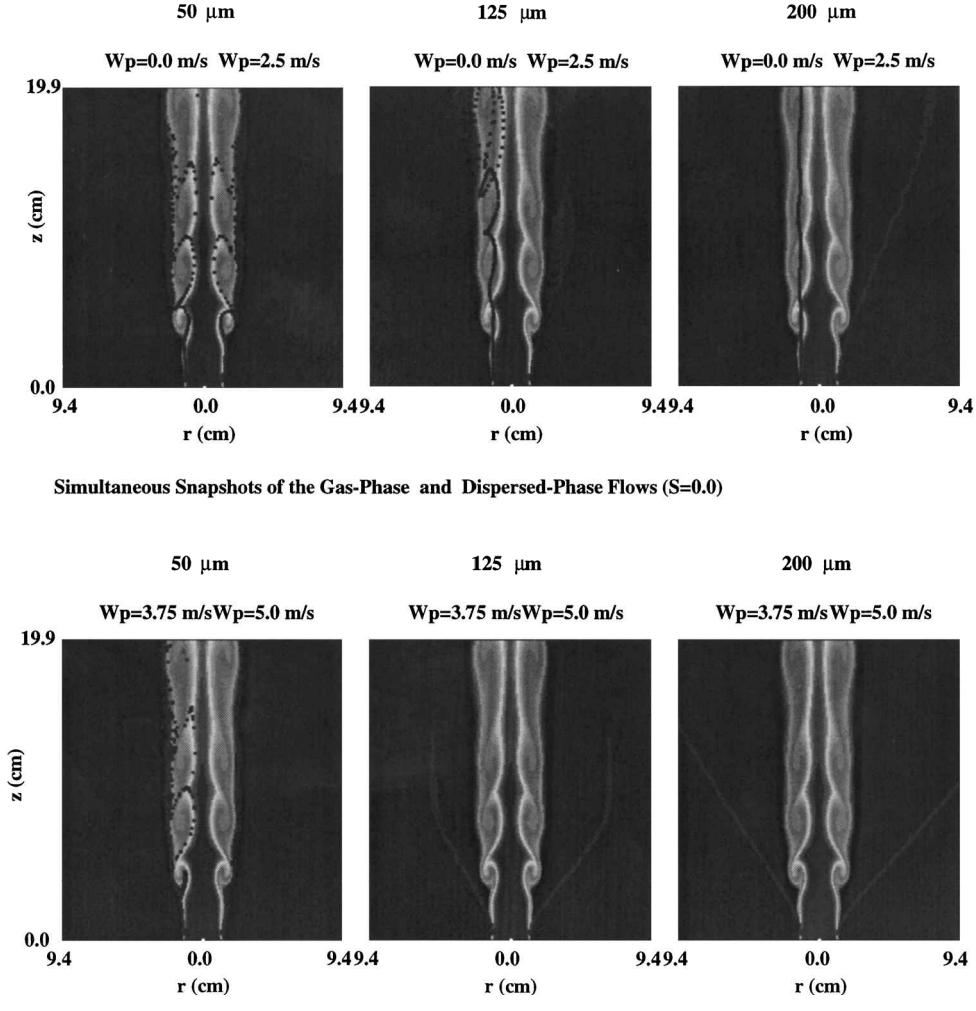


**Fig. 8 Computed images of the two-phase flowfield in terms of the instantaneous isotemperature contours and locations of nonevaporating droplet with different initial swirl velocity injected in the nonswirling jet.**

**Effect of Swirl Injection Velocity on Droplet Dispersion**

For the results presented so far, the droplets were injected with zero initial swirl velocity. Because many applications involve droplet injection with a finite swirl velocity, it is of interest to examine the effect of initial swirl on droplet transport. Figure 8 shows instantaneous images of the two-phase flow, highlighting the effect of the azimuthal injection velocity on droplet dispersion in a nonswirling jet. The nonevaporating droplets having the same axial velocity (5 m/s) and different initial swirl velocities ($w_p = 0$, 2.5, 3.75, and 5 m/s) are injected into the nonswirling heated air jet. Three droplet sizes are included, representing the small, intermediate, and large Stokes numbers. As expected, the dispersion of smaller droplets ($d_k \leq 50\ \mu$m) is mainly governed by the dynamics of large vortex rings irrespective of the initial swirl velocity, whereas that of larger droplets ($d_k > 150\ \mu$m) is essentially governed by their injection parameters and not by the vortex ring dynamics. On the other hand, the dispersion of intermediate-size droplets ($d_k = 125\ \mu$m) is governed by both the vortex ring dynamics and initial swirl velocity.

## Conclusions

We have investigated the dispersion of nonevaporating and evaporating droplets in a swirling, heated jet. The transient characteristics of the swirling jet including the dynamics of large vortex rings have been computed by using a direct numerical solver[18] for the Navier–Stokes and energy equations without any turbulence or subgrid model. The droplet transport has been simulated by using a Lagrangian approach. Simulations have been validated by establishing their grid independence and by comparing the predicted and measured Strouhal numbers. Detailed flow visualization based on the computed snapshots of two-phase flow, as well as quantitative results, has been employed to characterize the effects of swirl and vaporization on droplet dispersion in the near jet region.

Results for nonevaporating droplets in both nonswirling and swirling jets indicate a nonmonotonic dispersion behavior, with the maximum dispersion occurring near Stokes number of unity. Whereas this behavior for nonswirling jets has been reported previously, that for swirling jets is observed for the first time. This, of course, is an expected result because in the absence of small-scale turbulence, the flow time is determined by the vortex time for both nonswirling and swirling jets. Our results indicate that the dynamic interactions of droplets with large vortex rings is an important phenomenon in the near region of both nonswirling and swirling shear flows. However, the vortex ring dynamics is strongly modified by swirl, leading to strong pairing interactions and changes in their dominant frequency. This significantly enhances dispersion compared to that in the nonswirling jet over the entire droplet size range. In addition, the relative enhancement becomes greater as the swirl number is increased. There are, however, important differences with regard to the mechanism contributing to higher dispersion for different-size droplets. For small droplets including gas particles (small Stokes number), the higher dispersion appears to be caused by the increased rate of shear layer growth at higher swirl numbers. For intermediate-size droplets, $\mathrm{St} \sim \mathcal{O}(1)$, the increased dispersion is believed to be caused by the strong vortex pairing interactions and by the transfer of swirl velocity from the gas phase to the droplets. Note that the enhanced particle dispersion caused by vortex pairing interactions has been observed in previous experimental[1,2] and computational[3,4] studies. For larger droplets (large Stokes number), the higher dispersion is essentially due to the transfer of swirl velocity from the gas phase to the droplets.

The effect of vaporization on droplet dispersion is characterized in terms of the droplet lifetime compared to its response time and the characteristic flow (vortex) time. For the conditions investigated, the dispersion of evaporating droplets is noticeably reduced compared to the nonevaporating case. In addition, the dispersion function vs Stokes number plot, especially the size-selective behavior, is modified by vaporization. Droplets with a diameter less than the optimum value (corresponding to the maximum dispersion) are sufficiently vaporized during their interaction with the vortex rings, such that their dispersion behavior approaches the low Stokes number limit. In this region, the droplet lifetime is of the same order of magnitude as the vortex time. On the other hand, the droplets with diameter higher than the optimum value are not vaporized significantly because their lifetime is significantly higher than the vortex time. Consequently, their dispersion follows the large Stokes number behavior, though the dispersion function value is reduced due to vaporization.

Finally, the effect of injection swirl velocity indicates that by imparting initial swirl to droplets at the point of injection can significantly modify the dispersion of intermediate-size [$\mathrm{St} \sim \mathcal{O}(1)$] and large-size (large Stokes number) droplets. However, the dispersion of small droplets is essentially governed by the gas-phase swirl and vortex ring dynamics.

Note that this is the first study dealing with droplet dispersion in a transient swirling jet in the context of large vortex structures. The present results clearly indicate that the shear-layer dynamics in two-phase, coflowing, swirling jets is a complex and rich phenomenon, and there are several aspects that need to be examined further. In particular, the effects of corotating and counter-rotating swirl on shear-layer stability, vortex dynamics, and droplet dispersion should be investigated using simulations and laboratory experiments.

## Acknowledgments

This work was in part funded by the U.S. Air Force Office of Scientific Research under Grant F49620-93-1-0400 monitored by Julian M. Tishkoff. T. W. Park was supported by a National Research Council Fellowship. Computations were performed on the Cray C-90 at the Pittsburgh Supercomputing Center and SGI Power Challenge at the National Computational Science Alliance.

## References

[1] Longmire, E. K., and Eaton, J. K., "Structure of a Particle-Laden Round Jet," *Journal of Fluid Mechanics*, Vol. 236, 1992, pp. 217–257.

[2] Lazaro, B. J., and Lasheras, J. C., "Particle Dispersion in the Developing Free Shear Layer, Part 1—Unforced Flow," *Journal of Fluid Mechanics*, Vol. 235, 1992, pp. 143–178.

[3] Crowe, C. T., Chung, J. N., and Trout, T. R., "Particle Mixing in Free Shear Flows," *Progress in Energy and Combustion Science*, Vol. 14, No. 3, 1988, pp. 171–194.

[4] Uthuppan, J., Aggarwal, S. K., Grinstein, F. F., and Kailasanath, K., "Particle Dispersion in a Transitional Axisymmetric Jet: A Numerical Simulation," *AIAA Journal*, Vol. 32, No. 10, 1994, pp. 2004–2014.

[5] Aggarwal, S. K., "Relationship Between the Stokes Number and Intrinsic Frequencies in Particle-Laden Flows," *AIAA Journal*, Vol. 32, No. 6, 1994, pp. 1322–1325.

[6] Chang, E., and Kailasanath, K., "Simulation of Dynamics in a Confined Shear Flow," *AIAA Journal*, Vol. 34, No. 6, 1996, pp. 1160–1166.

[7] Longmire, E. K., and Eaton, J. K., "Active Open-Loop Control of Particle Dispersion in Round Jets," *AIAA Journal*, Vol. 32, No. 3, 1994, pp. 555–563.

[8] Lazaro, B. J., and Lasheras, J. C., "Particle Dispersion in the Developing Free Shear Layer, Part 2—Forced Flow," *Journal of Fluid Mechanics*, Vol. 235, 1992, pp. 179–221.

[9] Aggarwal, S. K., and Xiao, Y., "Effect of External Forcing on Droplet Dispersion in a Developing Shear Flow," *Journal of Propulsion and Power*, Vol. 10, No. 3, 1994, pp. 395–401.

[10] Uthuppan, J., and Aggarwal, S. K., "Particle Dispersion Enhancement in the Near Region of a Forced Jet," *Journal of Propulsion and Power*, Vol. 15, No. 2, 1999, pp. 266–271.

[11] Lilly, D. G., "Swirling Flows in Combustion: A Review," *AIAA Journal*, Vol. 15, No. 8, 1977, pp. 1063–1078.

[12] Ribeiro, M. M., and Whitelaw, J. H., "Coaxial Jets with and Without Swirl," *Journal of Fluid Mechanics*, Vol. 96, 1980, pp. 769–795.

[13] Leschziner, M. A., and Rodi, W., "Computation of Strongly Swirling Axisymmetric Jets," *AIAA Journal*, Vol. 22, No. 12, 1984, pp. 1742–1747.

[14] Sommerfeld, M., and Qiu, H.-H., "Characterization of Particle-Laden, Confined Swirling Flows by Phase-Doppler Anemometry and Numerical Calculation," *International Journal of Multiphase Flow*, Vol. 19, No. 6, 1993, pp. 1093–1127.

[15] Gupta, A. K., Presser, C., Hodges, J. T., and Avedisian, C. T., "Role of Combustion on Droplet Transport in Pressure-Atomized Spray Flames," *Journal of Propulsion and Power*, Vol. 12, No. 3, 1996, pp. 543–553.

[16] Feikema, D. A., Eskridge, R., and Hutt, J. J., "Structure of a Nonevaporating Swirl Injector Spray," *Atomization and Sprays*, Vol. 7, No. 1, 1997, pp. 77–95.

[17] Park, T. W., Aggarwal, S. K., and Katta, V. R., "On the Dynamics of a Two-Phase Swirling Jet," *International Journal of Multiphase Flow*, Vol. 24, No. 2, 1998, pp. 295–317.

[18]Katta, V. R., Goss, L. P., and Roquemore, W. M., "Effect of Nonunity Lewis Number and Finite-Rate Chemistry on the Dynamics of a Hydrogen–Air Jet Diffusion Flame," *Combustion and Flame*, Vol. 96, Nos. 1/2, 1994, pp. 60–74.

[19]Leonard, B. P., "A Stable and Accurate Convective Modeling Procedure Based on Quadratic Upstream Interpolation," *Computer Methods in Applied Mechanics and Engineering*, Vol. 19, No. 1, 1979, pp. 59–98.

[20]Spalding, D. B., "A Novel Finite Difference Formulation for Difference Expressions Involving Both First and Second Derivatives," *International Journal for Numerical Methods in Engineering*, Vol. 4, 1972, pp. 551–559.

[21]Lazaro, B. J., and Lasheras, J. C., "Particle Dispersion in a Turbulent, Plane, Free Shear Layer," *Physics of Fluids A*, Vol. 1, No. 6, 1989, pp. 1035–1050.

[22]Renksizbulut, M., and Yuen, M. C., "Numerical Study of Droplet Evaporation in a Viscous Fluid," *Journal of Heat Transfer*, Vol. 105, 1983, pp. 389–395.

[23]Sirignano, W. A., "Fluid Dynamics of Sprays—1992 Freeman Scholar Lecture," *Journal of Fluids Engineering*, Vol. 115, 1993, pp. 345–378.

[24]Faeth, G. M., "Evaporation and Combustion of Sprays," *Progress in Energy and Combustion Science*, Vol. 9, 1983, pp. 1–76.

[25]Park, T. W., Aggarwal, S. K., and Katta, V. R., "Gravity Effects on the Dynamics of Evaporating Droplets in a Heated Jet," *Journal of Propulsion and Power*, Vol. 11, No. 3, 1995, pp. 519–528.

J. R. Bellan
*Associate Editor*